Environmental Science and Ecotechnology 31 (2026) 100704

Contents lists available at ScienceDirect

Environmental Science and Ecotechnology

journal homepage: www.journals.elsevier.com/environmental-science-and-ecotechnology/

Original Research

Electron transfer drives hydroxyl radical formation in peroxone reactions

Yishi Wang, Wei Qiu *, Yongbo Yu, Jun Ma **

State Key Laboratory of Urban Water Resource and Environment, School of Environment, Harbin Institute of Technology, Harbin, 150090, China

ARTICLE INFO

Article history:
Received 5 September 2025
Received in revised form
30 April 2026
Accepted 2 May 2026

Keywords:
Ozone
Hydrogen peroxide
Hydroxyl radical yield
Marcus electron transfer
Ozone chain mechanism

ABSTRACT

Ozone is a powerful oxidant widely used in water treatment for the degradation of organic pollutants and removal of colour, odor, and pathogens. In aqueous solution, ozone decomposes to generate hydroxyl radicals through chain reactions that are accelerated by the addition of hydrogen peroxide in the peroxone process. Yet the precise initiation mechanisms of these chains and the efficiency of hydroxyl radical production have remained controversial, with prior models proposing adduct formation as the rate-limiting step and yielding only approximately 50% hydroxyl radicals in peroxone process. Here we show that the hydroxyl radical yield in the peroxone reaction is approximately 67%, substantially higher than previously reported. Through complete-capture scavenger assays, competition experiments, and high-precision quantum-chemical calculations informed by Marcus electron-transfer theory, we establish that ozone reacts with hydroxide exclusively by oxygen-atom transfer, while its reaction with the hydroperoxide anion proceeds through parallel electron transfer (approximately 50%) and oxygen-atom transfer (approximately 50%) pathways. Spin-orbit coupling enables spin-forbidden release of triplet oxygen in the atom-transfer channel. We also determine the pK_a of the hydroxyl radical precursor hydrotrioxide as approximately 6.15 and quantify the long-disputed hydroxyl radical–ozone reaction rate constant as 1.1×10^8 M^{-1} s^{-1}. These results revise classical ozonation and peroxone mechanisms and provide a mechanistic foundation for optimizing ozone-based advanced oxidation technologies for water purification.

1. Introduction

Ozone (O_3, C_{2v}) is an unusual oxidant with distinctive electronic and structural properties. It can be described as $O(O)_2$ or $O_2(^1\Delta_g) + O(^1D)$ [1] and exhibits 33% diradical character together with a hidden Jahn–Teller effect, with a bond length of 1.278 Å and a bond angle of 116.8°. Mixing of the O–O bond wavefunctions lower the singlet-state energy beyond the exchange energy associated with the triplet wavefunction, such that the ground state is a spin-polarized singlet [2–4]. O_3 has attracted considerable attention due to its ubiquitous presence in the air and its strong performance in water treatment [5,6]. In this context, O_3-based oxidation technology is widely used for the degradati on of organic pollutants, disinfection, and the removal of color and odor [7–9]. In water, O_3 can generate hydroxyl radicals (•OH) via H_2O-induced chain reaction that the essence of the reaction is the interaction with deprotonated OH^- (ozonation, $k_{H_2O,\ O_3} < 10^{-7}$ M^{-1} s^{-1}, $k_{OH^-,\ O_3} = 70$ M^{-1} s^{-1}). The addition of hydrogen peroxide (H_2O_2) would accelerate O_3 decay (peroxone, $k_{H_2O_2,\ O_3} < 10^{-2}$ M^{-1} s^{-1}), which is dominated by deprotonated HO_2^- ($k_{HO_2^-,\ O_3} = 5.5 \times 10^6$ M^{-1} s^{-1}) [10,11]. In O_3-based water treatment, adding H_2O_2 is one of the most effective methods for enhancing the O_3 efficiency [12,13]. The original mechanism of O_3 decay induced by OH^- and HO_2^- were suggested as equations (1)–(6) [10]:

$$O_3 + OH^- \rightarrow O_2 + HO_2^- \quad (1)$$

$$O_3 + HO_2^- \rightarrow O_3^{\cdot-} + HO_2^{\cdot} \quad (2)$$

$$HO_2^{\cdot} \rightleftharpoons O_2^{\cdot-} + H^+ \quad (3)$$

* Corresponding author.
** Corresponding author.
E-mail addresses: qiuweihit@126.com (W. Qiu), majun@hit.edu.cn (J. Ma).

https://doi.org/10.1016/j.ese.2026.100704

$$O_2^{\cdot-} + O_3 \rightarrow O_2 + O_3^{\cdot-} \quad (4)$$

$$O_3^{\cdot-} + H^+ \rightleftharpoons HO_3^{\cdot} \quad (5)$$

$$HO_3^{\cdot} \rightarrow \cdot OH + O_2 \quad (6)$$

Subsequently, the chain mechanism was revised to equations (7)–(16) [14]:

$$OH^- + O_3 \longrightarrow HO_4^- \quad (7)$$

$$HO_4^- \longrightarrow HO_2^- + O_2 \quad (8)$$

$$HO_4^- \longrightarrow HO_2^{\cdot} + O_2^{\cdot-} \quad (9)$$

$$H_2O_2 \rightleftharpoons HO_2^- + H^+ \quad (10)$$

$$HO_2^- + O_3 \longrightarrow HO_5^- \quad (11)$$

$$HO_5^- \rightarrow HO_2^{\cdot} + O_3^{\cdot-} \quad (12)$$

$$HO_5^- \rightarrow 2^3O_2 + OH^- \quad (13)$$

$$O_3^{\cdot-} \rightleftharpoons O_2 + O^{\cdot-} \quad (14)$$

$$O^{\cdot-} + H_2O \rightleftharpoons \cdot OH + OH^- \quad (15)$$

$$\cdot OH + O_3 \longrightarrow HO_2^{\cdot} + O_2 \quad (16)$$

In the course of insight into the •OH formation and O_3 decay, early mechanisms have suggested that OH^- in water initiates O_3 to produce HO_2^-, which further activates O_3 to generate •OH, corresponding to a 100% theoretical •OH yield [10]. However, the subsequent research found that the •OH yield was significantly lower than 100%, prompting a revision of the mechanism. The initial reaction O_3 with OH^- and HO_2^- involves adduct formation [15,16], and adduct formation has been proposed as the rate-determining step, limiting the •OH yield in the O_3/H_2O_2 (peroxone) process to only approximately 50% [15]. Although thermodynamic analyses have suggested possible pathways for O_3 attenuation caused by OH^- and HO_2^-, the role of adducts as chain-initiating intermediates remains controversial [17], and the specific O_3 chain initiation mechanism still needs further exploration. Meanwhile, the present studies primarily focus on pollutant degradation kinetics, with limited attention to the intrinsic conditions that influence the •OH yield in O_3-based reactions. In fact, pollutant removal efficiencies may appear similar under certain conditions, while degradation rates can vary significantly. In recent decades, theoretical calculations based on quantum chemical methods, particularly density functional theory (DFT), have become increasingly important in the study of advanced oxidation processes (AOPs) [18]. Theoretical calculations have emerged as a powerful auxiliary tool in environmental chemistry for material property characterization, elucidation of pollutant degradation pathways, and analysis of reaction processes [19]. However, the theoretical calculation of the chain decay of O_3 with a spin-polarized singlet state remains unclear. Therefore, in-depth insight into the chain mechanism of O_3 decay in aqueous solution in the presence of H_2O_2, combining experimental and theoretical calculations, should be pursued urgently.

Herein, we established a kinetic functional relationship between •OH exposure with pH value and H_2O_2 concentration. Using complete capture (tert-butanol [t-BuOH] and dimethyl sulfoxide [DMSO]) and competition assays (scavenger and probe), we determined the •OH yield of chain initiation in peroxone reaction and characterized the pH dependence of the •OH formation in the O_3/OH^- process. Moreover, we investigated the chain initiation mechanisms of O_3 decomposition induced by OH^- and HO_2^- based on high-precision quantum chemistry and thermodynamic calculations. In addition, we further quantified the pK_a of the •OH precursor $HO_3^{\bullet}$ and resolved the long-disputed chain propagation rate constant between •OH and O_3 in aqueous solution. This study aims to provide a theoretical insight into better understanding and applying O_3-based oxidation.

2. Materials and methods

2.1. Chemicals and reagents

All reagents were purchased from Shanghai Aladdin Biochemical Technology Co., Ltd. (Shanghai, China), Tedia high-purity solvents Co., Ltd. (Anqing, Anhui province, China), or Sigma-Aldrich Co., Ltd. (Darmstadt, Germany) Solutions were prepared using the Milli-Q ultrapure water process (resistivity ≥18.2 MΩ cm). Detailed chemical information is provided in Supplementary Text S1.

2.2. Experimental procedures

The O_3 stock solution was determined spectrophotometrically at 260 nm (ε[260 nm] = 3200 M^{-1} cm^{-1}). The bottle cap was sealed to prevent volatilization, in which the reactors had almost no headspace. All experiments were conducted at 20 ± 1 °C, and the yield was determined in triplicate. Detailed information is provided in Supplementary Text S2.

2.3. Analytical methods

O_3 concentrations were measured using the indigo method [20]. We used an ultra-performance liquid chromatograph (LC300, PerkinElmer, Massachusetts, America) to analyze concentrations of ATZ (atrazine), *p*CBA (*p*-chlorobenzoic acid), *p*NBA (*p*-nitrobenzoic acid), NB (nitrobenzene), and BA (benzoic acid). Hydrogen peroxide was quantified via an N,N-diethyl-*p*-phenylenediamine (DPD) assay [21]. Oxidation products of dimethyl sulfoxide (DMSO) by •OH (methanesulfinic acid and methanesulfonic acid) were detected using high-performance ion chromatography (IC6200, Wayeal, Hefei, Anhui province, China). Detailed information is provided in Supplementary Text S3.

2.4. Quantum chemical calculations

The theory calculations were performed in ORCA 5.0.4 [22], the wavefunction analysis was accomplished in Multiwfn 3.8 dev [23–25], the charge transfer molecular configuration search calculations were carried out on the Molclus 1.12 [26], and molecular visualization in VMD 1.9.3 [27], The spin-polarized singlet ground state of O_3 exhibits a strong electronic correlation, requiring a wavefunction stability test to guarantee spontaneous symmetry-breaking wavefunction. Detailed information is provided in Supplementary Texts S4–S5.

3. Results and discussion

3.1. Organic pollutants degradation of in ozonation (O_3/H_2O) and peroxone (O_3/H_2O_2) processes

O_3 degrades organic pollutants via two pathways: (1) direct oxidation of O_3 molecules and (2) oxidation by the •OH generated during ozonation and peroxone (initiator structure is shown in

Fig. 1a). To identify the generation of the •OH in the O_3 system, terephthalic acid (THA) was used as an •OH trapping agent and produced stable fluorescent 2-hydroxyterephthalic acid (HTA) [28]. O_3 in water undergoes OH^--initiated chain reactions and produces •OH as an active intermediate [29] (Fig. 1b). Moreover, H_2O_2 can also induce O_3 chain reaction to generate •OH [30] (Fig. 1c). In real water treatment, O_3 decomposition is complex, with background organics acting as either inhibitors or promoters according to their contribution to O_3 decomposition [31]. To simplify, we added known inhibitors (acetate) and promoters (methanol and MeOH) to simulate real water matrices [32]. We further investigated •OH-mediated organic pollutant removal in the O_3-based system under specific background conditions, and atrazine (ATZ) was selected as the target compound ($k_{ATZ,•OH} = 3.0 \times 10^9\ M^{-1}\ s^{-1}$, $k_{ATZ,\ O_3} = 6.0\ M^{-1}\ s^{-1}$). For an initial O_3 concentration of 25 μM, the half-life of the ATZ reduction caused by O_3 alone exceeds 111 min [33]. ATZ decay was enhanced by increasing pH (Fig. 1d) and by the addition of H_2O_2 (Fig. 1e), indicating that both methods accelerated •OH generation. Meanwhile, the depletion rate of O_3 was also greatly accelerated (Supplementary Fig. S1). Except for ATZ, similar phenomena were observed in different types of organic pollutants, such as nitrobenzene (nitro-compound), 2,4-dichlorophenoxyacetic acid (chlorinated organic, $pK_a = 2.64$), and benzoic acid (organic weak acids, $pK_a = 4.19$), which further confirmed the universal conclusion that OH^- and H_2O_2 enhanced O_3 to produce •OH, and intensified the degradation of organic pollutants (Supplementary Fig. S2).

On this basis, the O_3 decay kinetics were carried out (Fig. 1f and g). The t-BuOH and CCl_4 react with •OH and $O_2^{\bullet-}$, with rate constants of $k_{•OH,\ t\text{-}BuOH} = 6.0 \times 10^8\ M^{-1}\ s^{-1}$ and $k_{O_2^{\bullet-},\ CCl_4} = 1.1 \times 10^9\ M^{-1}\ s^{-1}$, respectively, thereby reducing O_3 consumption [32,34] while the MeOH promote O_3 attenuation. Reported rate constants for the reactions of O_3 with •OH and $O_2^{\bullet-}$ are $k_{•OH,O_3} = (0.1\text{–}3.0) \times 10^9\ M^{-1}\ s^{-1}$ [35,36] and $k_{O_2^{\bullet-},\ O_3} = 1.6 \times 10^9\ M^{-1}\ s^{-1}$ [37], respectively. Accordingly, at an initial CCl_4 concentration of 4.0 mM, the capture rate of $O_2^{\bullet-}$ up to $6.4 \times 10^6\ s^{-1}$, whereas at 2.0 mM, the scavenging rate of •OH reaches $1.2 \times 10^6\ s^{-1}$. In terms of the scavenging rate, CCl_4 inhibits O_3 attenuation more than t-BuOH at the same concentration. However, the actual inhibitory effect of CCl_4 on O_3 decay is very weak, and even 5 μM t-BuOH shows much greater inhibition than 1 mM CCl_4 (Fig. 1h and i). Thus, the visible fact that CCl_4 weakens O_3 decrease is not the role of the real CCl_4 body. In addition, the O_3

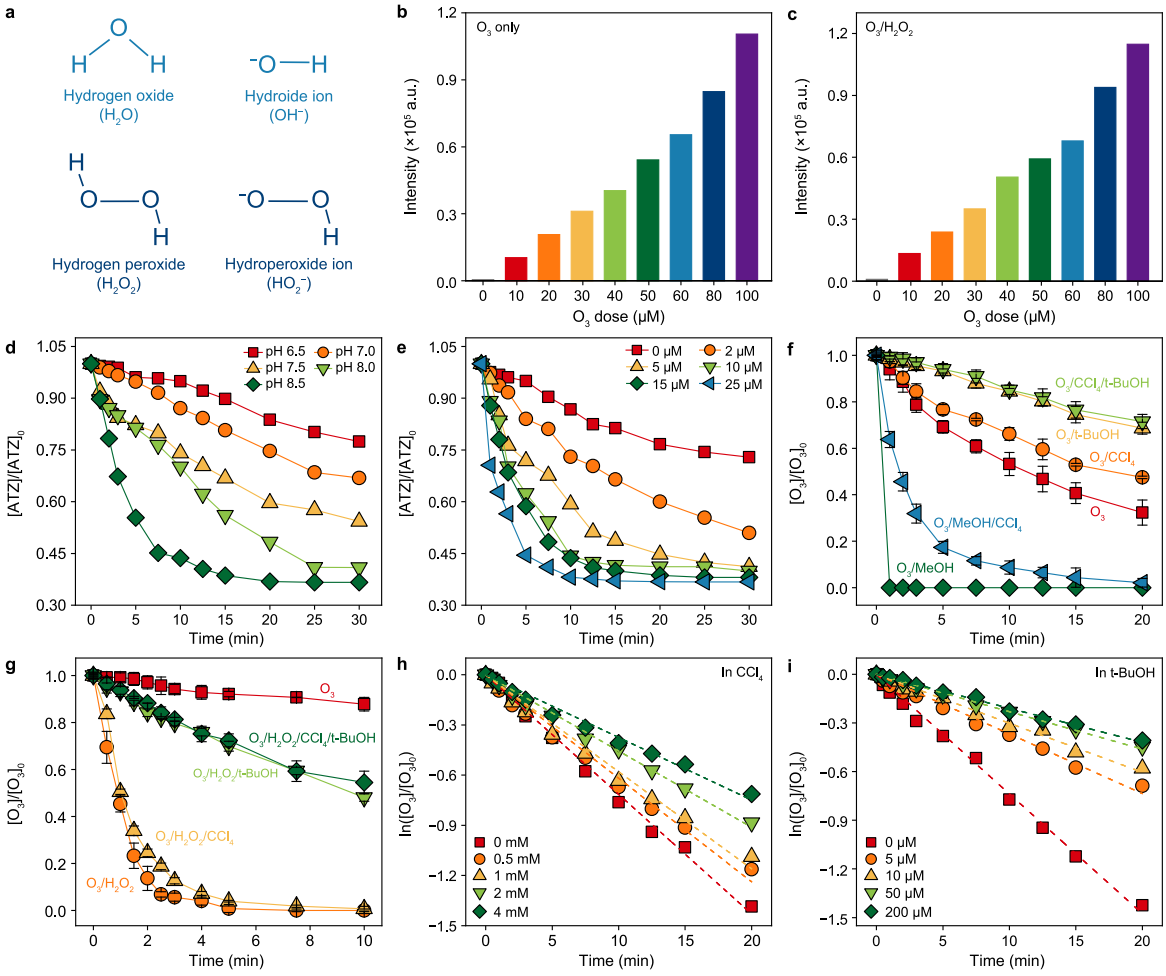

Fig. 1. Hydroxyl radical-mediated pollutant degradation and ozone decay in ozonation and peroxone processes. a, Structures of H_2O, OH^-, H_2O_2 and HO_2^-. **b**–**c**, Fluorescence intensity of HTA concerning O_3 dose in the O_3-only (**b**) and O_3/H_2O_2 (**c**) processes. **d**–**e**, Time-dependent attenuation of ATZ in the O_3-only process at pH 6.5–8.5 (**d**) and in the O_3/H_2O_2 process at pH 7.0 (**e**). **f**–**g**, Effects of inhibitors and promoters on O_3 decay of O_3-only (**f**) and O_3/H_2O_2 (**g**) processes. **h**–**i**, Concentration effect of CCl_4 (**h**) and t-BuOH (**i**) on O_3 decay. Conditions: $\lambda_{ex} = 315$ nm, $\lambda_{em} = 425$ nm, [THA] = 0.5 mM; $[O_3]_0 = 50$ μM, $[H_2O_2]_0 = 0.5$ mM for panels **b** and **c**; $[O_3]_0 = 25$ μM, [MeOH] = 35 μM, [Acetate] = 175 μM, and $[ATZ]_0 = 1$ μM for panels **d** and **e**; $[CCl_4]_0 = 4.0$ mM, $[t\text{-BuOH}]_0 = 2$ mM, $[MeOH]_0 = 0.2$ mM, pH 8.0 for panel **f**; pH 6.5 and $[H_2O_2]_0 = 50$ μM for panel **g**; $T = 20$ °C. O_3 decay of panels **f** and **g** were measured in three parallel repetitions, and error bars were derived from the standard deviation.

decay and ATZ removal rates in excess of the t-BuOH/CCl_4 and t-BuOH alone were nearly identical in both O_3 and O_3/H_2O_2 systems (Supplementary Fig. S3). The CCl_4, as an inhibitor of O_3 attenuation, was possibly only a kinetic artifact. The inhibition of the chain process was likely due to trace organic impurities in CCl_4, a phenomenon similar to that observed in previous studies [38,39]. The reported high kinetic isotope effect ($k_H/k_D = 19$) was attributed to the trace impurity in D_2O that inhibited O_3 chain decay, and as little as 0.25 μM of multiple oxidizable organic impurities could shorten the chain length to this extent. Therefore, the inhibitory effect of CCl_4 on O_3 decay should be attributed to the presence of oxidizable impurities.

3.2. R_{ct} values in ozonation and peroxone reactivity

The influence of OH^- concentration (ozonation) and H_2O_2 dose (peroxone) on •OH generation was assessed using the R_{ct} value. Here, R_{ct} was defined as the ratio of the •OH exposure to O_3 exposure in a given water [40]:

$$R_{ct} = \frac{\int [\cdot OH]dt}{\int [O_3]dt} \quad (17)$$

where $\int[\bullet OH]dt$ and $\int[O_3]dt$ individually represent the integrals of [•OH] and [O_3] with respect to time. The *p*-chlorobenzoic acid (*p*CBA) is an ideal probe that reacts slowly with O_3 ($k_{pCBA, O_3} < 0.9\ M^{-1}\ s^{-1}$) but rapidly with •OH ($k_{pCBA, \bullet OH} = 5.0 \times 10^9\ M^{-1}\ s^{-1}$) [41]. The •OH exposure was derived from the degradation of the probe compound *p*CBA (Supplementary Table S1), and O_3 exposure was calculated from the integral of the O_3 decay curve over time. Integrating equation (17) gives:

$$R_{ct} = -\frac{1}{k_{\cdot OH,pCBA}} \frac{\ln([pCBA]/[pCBA]_0)}{\int [O_3]dt} \quad (18)$$

R_{ct} can quantify the contribution of •OH to oxidation in the O_3 systems. We investigated the R_{ct} values across typical pH ranges and H_2O_2 doses on the O_3 decay process in synthetic solutions [32,40]. The pH affected O_3 chain attenuation and organic degradation through varying OH^- concentrations. The increase in pH prominently accelerated the O_3 reduction and probe *p*CBA degradation (Fig. 2a and b), fitted the O_3 decay curve using a pseudo-first-order model, and linearly fitted the natural logarithm of *p*CBA abatement with O_3 exposure to obtain R_{ct} values at pH 6.5–8.5 (Supplementary Fig. S4 and Table S2). The results indicate that R_{ct} is linearly related to the OH^- concentration for a given water (Fig. 2c). Moreover, this straight line passing through the origin indicates that R_{ct} becomes 0 when $[OH^-] = 0$ if H_2O-catalyzed O_3 decomposition ($k_{H_2O,O_3} < 10^{-7}\ M^{-1}\ s^{-1}$) is neglected [11]. This suggests that O_3 will remain in the molecular state rather than decay.

Similar tendencies in O_3 and *p*CBA decreases were also observed in the peroxone process at a fixed pH of 7.0, where slight H_2O_2 doses exhibited a significant acceleration effect (Fig. 2d and e; Supplementary Fig. S5 and Table S3). R_{ct} increased linearly with H_2O_2 dose (Fig. 2f), suggesting that H_2O_2 triggered the O_3 chain reaction to produce •OH and enhanced steady-state or transient •OH concentration. Moreover, the intercept R_{ct} of 7.3×10^8 at 0 μM H_2O_2 ($R_{ct} = 9.77 \times 10^8$ in the ozonation process at a pH = 7.0) shows that OH^- dominates the chain attenuation of O_3 to form •OH generation in this case. Therefore, increasing pH and adding H_2O_2 both enhance R_{ct}, thereby increasing the proportion of •OH in O_3 systems. Nonetheless, increasing pH theoretically enhances •OH-mediated oxidation, while the near-neutral pH and strong buffering capacity of real water systems limit practical implementation. Therefore, the addition of H_2O_2 is a more feasible strategy to promote •OH-mediated oxidation in O_3-based systems.

3.3. The •OH yield determination by complete capture assays in ozonation and peroxone reactivity

The •OH yield (Φ) is defined as the number of moles of •OH generated per mole of O_3 consumed. In complete capture assays, excess •OH-capturing agents, such as methanol, t-BuOH, and DMSO, are added to collect all generated •OH, which is then quantified by product analysis. The •OH reacts with methanol to form almost an equal amount of formaldehyde (HCHO) [42], in which derivative products of HCHO derived with 2,4-dinitrophenylhydrazine (2,4-DNPH) can be detected simply by using liquid chromatography. Methanol reacts negligibly with O_3 ($k_{O3,\ methanol} = 0.024\ M^{-1}\ s^{-1}$) [43], but it reacts rapidly with •OH ($k_{\bullet OH,\ methanol} = 9.7 \times 10^8\ M^{-1}\ s^{-1}$) [44] and generates chain promoter $O_2^{\bullet-}$ for O_3 chain propagation (equation (4); $k = 1.6 \times 10^9\ M^{-1}\ s^{-1}$). Thus, the methanol assay essentially records total •OH, including both chain initiation and propagation processes in ozonation [45]. The methanol assay results showed an •OH yield of approximately 0.97 (close to 1.0) in the O_3 reaction (Fig. 3a), while the •OH yield in the O_3/HO_2^- reaction was only 0.89, and it was almost unaffected by pH (Supplementary Fig. S6). As obtained above, H_2O_2 kinetically accelerated the conversion of O_3 to •OH, but the cumulative •OH yield in O_3/H_2O_2 process was lower than in the O_3-only process (0.89 < 0.97). The •OH scavenging rate of 0.5 mM H_2O_2 reached $1.35 \times 10^4\ s^{-1}$ ($k_{H_2O_2, \bullet OH} = 2.7 \times 10^7\ M^{-1}\ s^{-1}$) [34], which was far lower than the capture rate of $4.85 \times 10^7\ s^{-1}$ for 50 mM methanol. The discrepancy may arise from H_2O_2 consuming extra $O_3^{\bullet-}$ resulting in a decrease of •OH formation ($k_{H_2O_2,\ O_3^{\bullet-}} = 1.6 \times 10^6\ M^{-1}\ s^{-1}$).

The t-BuOH assay quantifies •OH via product analysis [46,47]. The •OH derives the reaction with t-BuOH and produces 2-hydroxy-2-methylpropanal (MHP), acetone, and HCHO ($k_{\bullet OH,\ t\text{-}BuOH} = 6.0 \times 10^8\ M^{-1}\ s^{-1}$, $k_{O_3,\ t\text{-}BuOH} = 3.0 \times 10^{-3}\ M^{-1}\ s^{-1}$), in which consumed •OH is about double the HCHO generated. Previous assays reported a maximum •OH yield of approximately 50% in the O_3/H_2O_2 process [15], while another study observed an •OH yield of 55% in O_3 alone at pH 10.5 [48], contradicting the general trend of $\Phi(O_3) < \Phi(O_3/H_2O_2)$ [45]. Thus, to determine the •OH yield in the O_3/OH^- and O_3/HO_2^- reactions, we re-examined the processes. Our t-BuOH measured •OH yields of 29.8% (O_3) and 68.4% (O_3/H_2O_2) relative to O_3 consumption at pH 7.0 and a temperature of 20 °C (Fig. 3b). Both yields (<100%) resulted from t-BuOH blocking the propagation of the O_3 chain reaction via scavenging •OH. Nevertheless, excess $O_2^{\bullet-}$ scavenger CCl_4 did not affect the •OH formation (Supplementary Fig. S7), which further verified the above "kinetic artifact" conclusion that organic impurities contained in CCl_4 reagent act as a kinetic inhibitor of O_3 decomposition. The t-BuOH assay quantified the •OH of the chain initiation process, in which 10 mM t-BuOH nearly eliminated all •OH (scavenging capacity: $k = 6.0 \times 10^6\ s^{-1}$) (Supplementary Fig. S8).

Further, we explored the influence of pH on •OH yields in the ozonation and peroxone reactions (Fig. 3c). The pH-dependent •OH yields in the O_3 alone process showed that the •OH yield increased from 16.9% to 60.1% over pH 6–11, while •OH formation of the peroxone was almost unaffected and maintained approximately 67.2%. At a pH of 10.5, the •OH yield (56.9%) in the ozonation alone was close to the reported 55% [48]. In addition, we noted that previous studies stated that the wall effect was primarily responsible for O_3 chain initiation and termination [49], but our results showed that the wall effect did not dominate •OH yields in the ozonation (Fig. 3d) and peroxone reactions (Fig. 3e) in the presence of excess scavenger (Supplementary Table S4).

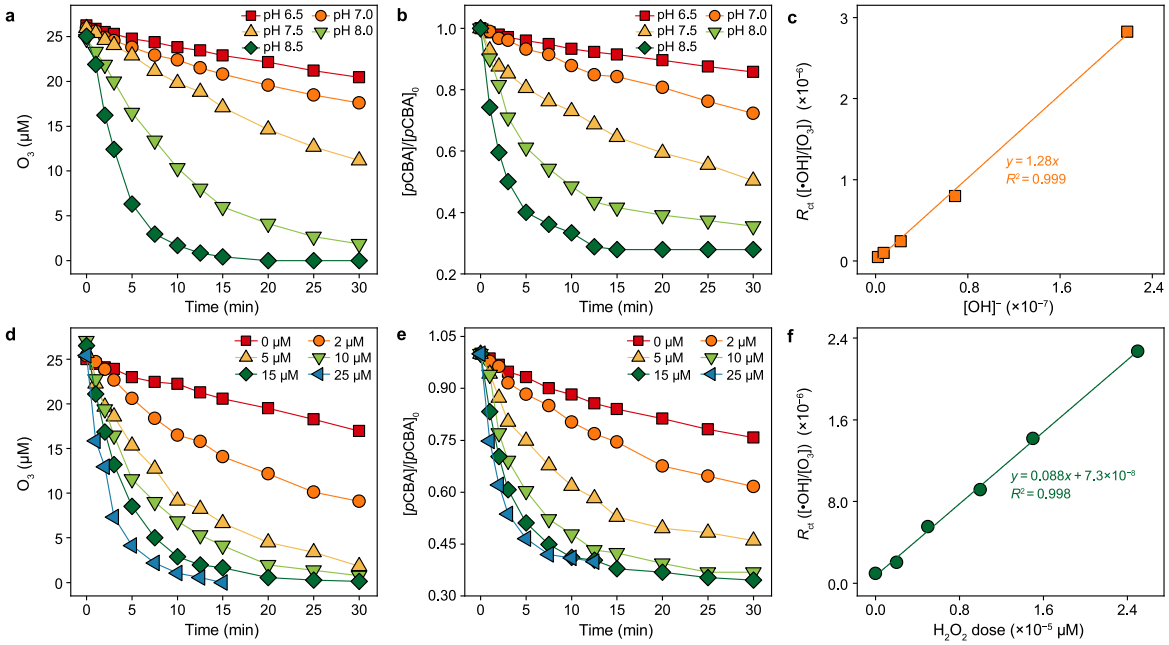

Fig. 2. R_{ct} ($\int$[•OH]dt/$\int$[O_3]dt) **values in the ozonation and peroxone reactions. a–b**, Time-dependent decay of O_3 (**a**) and *p*CBA (**b**) in the O_3-only process at different pH values. **c**, Relationship between the calculated R_{ct} value and the OH^- concentration in the O_3-only process. **d–e**, Time-dependent decay of O_3 (**d**) and *p*CBA (**e**) at different H_2O_2 doses in the O_3/H_2O_2 process. **f**, Relationship between the calculated R_{ct} value and H_2O_2 dose in the O_3/H_2O_2 process. Conditions: $[O_3]_0$ = 25 μM, $[pCBA]_0$ = 1 μM, [MeOH] = 70 μM, [Acetate] = 350 μM, and [PBS] = 4 mM for panels **a–c**; $[O_3]_0$ = 25 μM, $[pCBA]_0$ = 1 μM, [MeOH] = 70 μM, [Acetate] = 350 μM, and pH 7.0 for panels **d–f**.

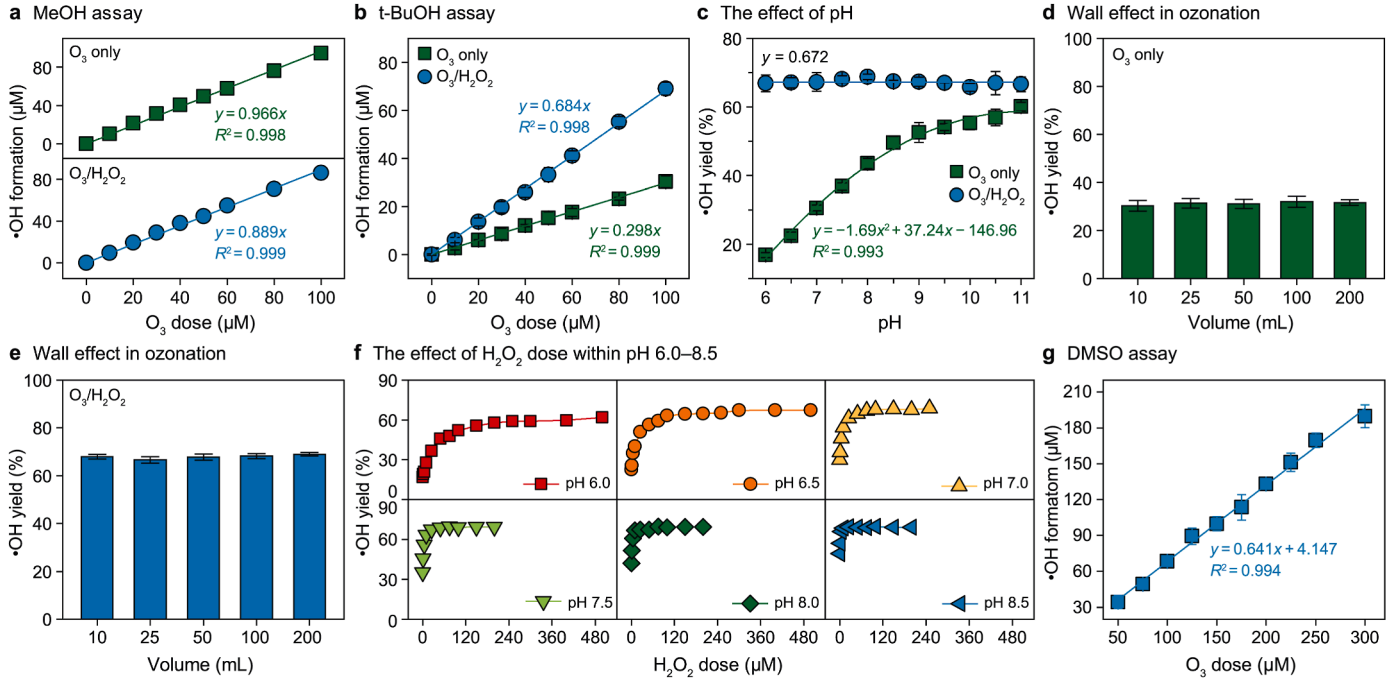

Fig. 3. Determination of •OH yield by complete capture assays. a–b, Methanol assay (**a**) and t-BuOH assay (**b**) of •OH formation as a function of O_3 dose in the O_3-only and O_3/H_2O_2 processes. **c**, Effect of pH on •OH yield in the O_3-only and O_3/H_2O_2 processes. **d–e**, The influence of wall effect on •OH yields in the O_3-only (**d**) and O_3/H_2O_2 processes (**e**). **f**, The change of •OH yield with H_2O_2 dose within at pH 6.0–8.5. **g**, •OH yield determined from methanesulfinic acid and methanesulfonic acid formation in the DMSO assay. Conditions: $[H_2O_2]$ = 0.5 mM, [PBS] = 4 mM, [MeOH] = 50 mM for panel **a**; [t-BuOH] = 50 mM for panels **b–f**; $[H_2O_2]$ = 0.5 mM for panels **a–c** and panel **e**; $[O_3]_0$ = 50 μM for panels **d–f**; pH 7.0 for panels **a–b** and panels **d–e**; [DMSO] = 75 mM, $[H_2O_2]$ = 25 mM, and pH 8.5 for panel **g**. Yield was measured in three parallel repetitions, and error bars were derived from the standard deviation.

Meanwhile, we broadened the numerical relationship between the •OH yield and H_2O_2 dose within pH 6.0–8.5 (Fig. 3f). Increasing pH reduced the H_2O_2 dose required to achieve •OH production (approximately 67%), and the ratio of H_2O_2:O_3 ranged from 10:1 reduced to less than 1:2 due to increased OH^- and deprotonated HO_2^-. In addition, the stoichiometric ratio between O_3 and H_2O_2

approached 1:1 without considering the interference of H_2O_2 generated by O_3 chain process (Supplementary Fig. S9), while the addition of t-BuOH would introduce additional H_2O_2 [46].

DMSO is another •OH scavenger used in complete-capture assays (equation (19)) [50]. It reacts with •OH to form methanesulfinic acid (92% yield) [15,51], but the methanesulfinic acid is further oxidized to methanesulfonic acid.

$$(CH_3)_2S{=}O + {\bullet}OH \rightarrow CH_3S(O)OH + {\bullet}CH_3 \quad (19)$$

However, DMSO reacts quickly with both O_3 ($k = 8.1\ M^{-1}\ s^{-1}$) and •OH ($k = 7.0 \times 10^9\ M^{-1}\ s^{-1}$) [51,52]; thus, this method is used exclusively for •OH determination in rapid, kinetic-like peroxone reactions. To ensure H_2O_2 has an absolute advantage in causing O_3 decay, we applied 75 mM DMSO to collect •OH (•OH capture rate: $k = 5.3 \times 10^8\ s^{-1}$) and 25 mM H_2O_2 (•OH scavenging rate: $k = 6.8 \times 10^5\ s^{-1}$) to initiate O_3. At pH 8.5 and 20 °C, the pseudo-first-order rate constant for O_3 attenuation by H_2O_2 was 109.22 s^{-1}, with $k_{apparent} = 5.5 \times 10^6[H_2O_2]_{total}10^{(pH-pK)}\ s^{-1}$, whereas that for DMSO was 0.61 s^{-1} [10]. Methanesulfinic acid and methanesulfonic acid were quantified by ion chromatography. Considering a 92% transformation rate, the plotted curve slope is 0.641, which indicates that •OH formation is a function of O_3 dose, demonstrating that the •OH formation accounts for 64.1% of O_3 consumption in the O_3/H_2O_2 reaction, as determined by the DMSO assay (Fig. 3g). This value was slightly lower than the approximately 67% of the t-BuOH assay due to the large inherent error in O_3 systems and the addition of low-temperature O_3 stock solutions reduced the reaction system temperature, resulting in a decrease in the •OH yield. In summary, in aqueous solution at pH 6.0–11.0, the •OH yield of O_3-only system follows the relationship $y = -1.69x^2 + 37.24x - 146.96$, whereas that in the O_3/H_2O_2 reaction stabilizes at approximately 67%.

3.4. Measurement of the •OH yield in the peroxone by competition method

The competition method simultaneously uses the scavenger t-BuOH (abbreviated as S) and the •OH probe (denoted as P) to quantify •OH formation [9,15]. The consumption of the probe is attributed solely to •OH:

$$d[P] = k_{\cdot OH,P}[\cdot OH][P]dt \quad (20)$$

Ignoring the radical-radical annihilation, •OH depletion in the O_3/H_2O_2 process is given as:

$$d[\cdot OH] = [\cdot OH]\left(k_{\cdot OH,S}[S] + k_{\cdot OH,P}[P] + k_{\cdot OH,H_2O_2}[H_2O_2] + k_{\cdot OH,O_3}[O_3]\right)dt \quad (21)$$

Integrating equations (20) and (21) yields:

$$d[P]\frac{k_{\cdot OH,S}[S] + k_{\cdot OH,P}[P] + k_{\cdot OH,H_2O_2}[H_2O_2] + k_{\cdot OH,O_3}[O_3]}{k_{\cdot OH,P}[P]} = d[\cdot OH] \quad (22)$$

The O_3 decay follows the pseudo-first-order model. Considering the rapid O_3 decay and simplifying the calculation, the O_3 concentration was reasonably simplified as the average value of O_3 dose and final value ($[O]_{final} = 0$), and was regarded as a constant. The t-BuOH and H_2O_2 were excessive and equal to the initial concentration (0.5 mM t-BuOH and H_2O_2, $k_{t\text{-}BuOH} + k_{H_2O_2} = 3.1 \times 10^5\ s^{-1}$), and integrating equation (22) gives:

$$([P]_0 - [P]_\infty) + \left(\frac{k_{\cdot OH,S}[S]_0 + k_{\cdot OH,H_2O_2}[H_2O_2]_0 + k_{\cdot OH,O_3}[O_3]_{AVG}}{k_{\cdot OH,P}}\right)\ln\left(\frac{[P]_0}{[P]_\infty}\right) = [\cdot OH]_0 = \Phi[O_3]_0 \quad (23)$$

As there is an uncertainty in the second-order rate constant of •OH and O_3, $k_{\bullet OH,\ O_3} = (0.1\text{–}3.0) \times 10^9\ M^{-1}\ s^{-1}$ [29,35,36], it needs to be reviewed again. We used probes such as ATZ, *p*CBA, *p*NBA, BA, and NB to determine the •OH yield (Supplementary Table S5; Fig. 4a–f).

The slope corresponds to the •OH yield. A consistent yield (approximately 67%, matching t-BuOH results) was obtained only with $k_{\bullet OH,\ O_3} = 1.1 \times 10^8\ M^{-1}\ s^{-1}$, which is an average yield of 71% across five probes. Theoretical analysis also supports this value (see below). Meanwhile, the influence of the selected rate constant between •OH and O_3 on the •OH yield determination is shown (Supplementary Fig. S10). At 0.5 mM t-BuOH, the •OH scavenging rate is $3.0 \times 10^5\ s^{-1}$. For an O_3 dose of 0.1 mM, the maximum •OH capture rate by O_3 reaches $3.0 \times 10^5\ s^{-1}$, comparable to that of t-BuOH. The rate also attains $2.0 \times 10^5\ s^{-1}$ even with the revised value of $k_{\bullet OH,\ O3} = 2.0 \times 10^9\ M^{-1}\ s^{-1}$ [29]. O_3 would therefore compete effectively with t-BuOH for •OH, and the additional consumption of •OH by O_3 would inevitably lower the apparent yield (equation (23)). These results support $k_{\bullet OH,O_3} = 1.1 \times 10^8\ M^{-1}\ s^{-1}$ as the more reasonable rate constant for •OH and O_3.

In addition, we employed the competition method to assess •OH in the presence of CCl_4. Consistent with previous kinetic and complete capture results, in the competition method, the added CCl_4 showed a much higher scavenging rate for $O_2^{\bullet-}$ compared to t-BuOH for •OH, but it did not affect the •OH yield (Supplementary Fig. S11). Only when the oxidizable organic trace impurities in CCl_4 scavenged the •OH, can it be reasonably explained that excessive CCl_4 can only slightly weaken the O_3 attenuation, so that the high t-BuOH concentration added in the presence of CCl_4 hardly affects the •OH yield.

3.5. Theoretical insight O_3 chain decay mechanism in aqueous solution initiated by hydroxide ion (OH^-) and hydroperoxide ion (HO_2^-)

3.5.1. The electronic structure and reaction characteristics of O_3 with OH^- and HO_2^-

Quantum chemical calculations provide in-depth insight into the mechanism of O_3 chain initiation. O_3 is a multireference molecule, and we first evaluated the static correlation of all possible reactants or intermediates involved in the O_3/H_2O and O_3/H_2O_2 reactions in the aqueous solution using the T_1 diagnostic [53] from the coupled cluster singles and doubles model (CCSD) (Supplementary Table S6):

$$T_1 = \frac{\|t_1\|}{\sqrt{N_{elec}}} \quad (24)$$

Where $||t_1||$ is the Euclidean norm of the single excitation amplitude vector of the coupled cluster wave function, and N_{elec} represents the number of electrons involved in the calculation. O_3 has a T_1 diagnostic of 0.028 (threshold 0.020), which means that the electronic static correlation is non-negligible, and its orbitals would undergo degeneracy. Except for O_3, $O_3^{\bullet-}$, $HO_3^{\bullet}$, and $HO_2^{\bullet}$ radicals also have a strong static correlation (T_1 diagnostic = 0.034, 0.040, and 0.029). The molecular spin and charge distribution of O_3 was further evaluated (Fig. 5a). The ground state of O_3 is a spin-

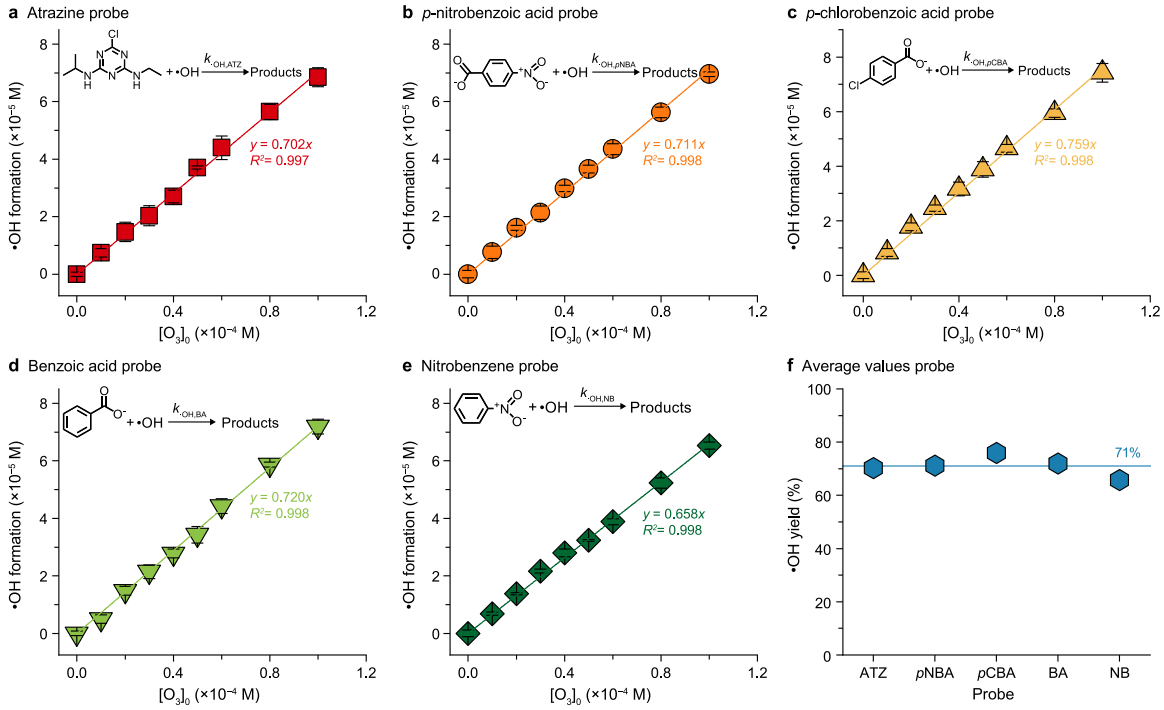

Fig. 4. The •OH yield determined by competition assay using t-BuOH and probe compounds. a–e, Linear relationships used to derive •OH yield from competition experiments with ATZ (**a**), *p*NBA (**b**), *p*CBA (**c**), BA (**d**), and NB (**e**). **f**, Summary of the •OH yields obtained from the five probe compounds. Conditions: $[ATZ]_0 = [pNBA]_0 = [pCBA]_0 = [BA]_0 = [NB]_0 = 1$ μM, $[H_2O_2]_0 = 0.5$ mM, $[t\text{-BuOH}]_0 = 0.5$ mM, pH = 7.0.

polarized singlet in which the central O-atom exhibits a positive charge (0.24), and the two terminal O-atoms have the same negative charge (−0.12). Opposite spins on terminal O-atoms ($|\alpha-\beta| = 0.51$) cause asymmetric HOMO (highest occupied molecular orbital) and LUMO (lowest unoccupied molecular orbital) contributions, resulting in a weak dipole moment of 0.53 Debye [2]. As O_3 has a degenerate ground-state electron structure, methods such as HF, DFT, and MP2, based on a single Slater determinant, perform poorly [54]. Our calculation supported this point (Fig. 5b), using the multireference configuration interaction method with the Davidson correction (MRCI + Q) as the benchmark. Common density functional theory (DFT) and the Hartree-Fock (HF) method both failed the energy calculation test; the errors exceeded 50 kcal mol^{-1}. The coupled cluster CCSD(T) is regarded as a "gold standard" in single-reference systems, and multireference methods have demonstrated excellent performance, consistent with previous studies [54]. For molecular optimization, DFT with a low proportion of HF exchange was sufficiently reliable, whereas calculations at the CASPT2(6,6)/def2-TZVPP level gave a bond length of 1.270 Å and a bond angle of 116.80°, respectively (Supplementary Table S7). The error of further high-level energy calculation based on the above structures was completely acceptable (Supplementary Fig. S12). Multireference calculations are thus critical for obtaining accurate energies on the potential energy surface of the O_3 reaction [55]. Furthermore, the frontier molecular orbitals (HOMO and LUMO) of O_3 with H_2O and H_2O_2 (including deprotonated forms) were investigated to predict electron transfer tendency at the B3LYP/def2-TZVPP level (Fig. 5c) [56]. Deprotonated OH^- and HO_2^- showed elevated HOMO energies compared with the molecular state, while the gap between the HOMO of HO_2^- and LUMO of O_3 was just 0.43 eV, which meant the Lewis base enhanced the electron transfer (ET) potential from electron donor to O_3 (Supplementary Fig. S13).

Based on the above, the mechanism for the initial step of O_3 decay triggered by OH^- and HO_2^- were re-examined, respectively. Diradical properties of the O_3 caused a relatively higher high-spin triplet state mixing into the ground state ($S^2 = 0.35$, ideal biradical $S^2 = 1$, singlet $S^2 = 0$) and the energy ($S_0 \rightarrow S_1 = 2.28$ eV and $S_1 \rightarrow T_1 = 1.08$ eV) (Supplementary Fig. S14), which was in agreement with the multireference calculation experiment that O_3 had a low-lying excited state [57,58]. Moreover, there exists a pair of weakly overlapping π orbitals on the central atom and terminal atoms in the O_3 ($S = 0.16$) (Supplementary Fig. S15), and forming a triplet state only requires breaking the singlet coupling between the electrons in the two weakly overlapping orbitals [59]. However, the product of O_3 and O_3/H_2O_2 reactions in aqueous solution is triplet O_2 [60], the direct conversion from singlet to triplet is spin-forbidden, and studies have proposed theories to illustrate reactivity (equations (7)–(16)). Previous assumptions have proposed that O_3 first forms adducts with OH^- and HO_2^- and then decomposes along two pathways [14,16,54]. According to the chain reaction principle, the initiation process is the rate-limiting step in the overall reaction course. In addition, adduct formation is the rate-limiting step, with $(k_{\overline{OH},\,O_3)ini} \approx k_{\overline{OH},\,O3} = 70\ M^{-1}\ s^{-1}$ and $(k_{HO_2^-,\,O_3)ini} \approx k_{HO_2^-,\,O_3} = 5.50 \times 10^6\ M^{-1}\ s^{-1}$. However, thermodynamic and kinetic calculations appear insufficient to achieve these rates [17,61]. Furthermore, unlike the addition of O_3 and olefins that undergo visible structure changes and induce a high energy barrier, the addition of O_3 to OH^- and HO_2^- is a single chemical bond addition, and the structure undergoes no significant changes. This indicates that the energy barrier should be quite low, or the rate is close to diffusion control in water ($10^{10}\ M^{-1}\ s^{-1}$), but the actual rates are only approximately 10 and $10^6\ M^{-1}\ s^{-1}$. In addition, the adduct HO_4^- could be considered as being produced by the interaction of the $HO_2^\bullet$ and $O_2^{\bullet-}$ instead of the O_3+OH^- channel [17]. In fact, almost all bimolecular first form a complex before the reaction, which may be a chemical bond or an intermolecular

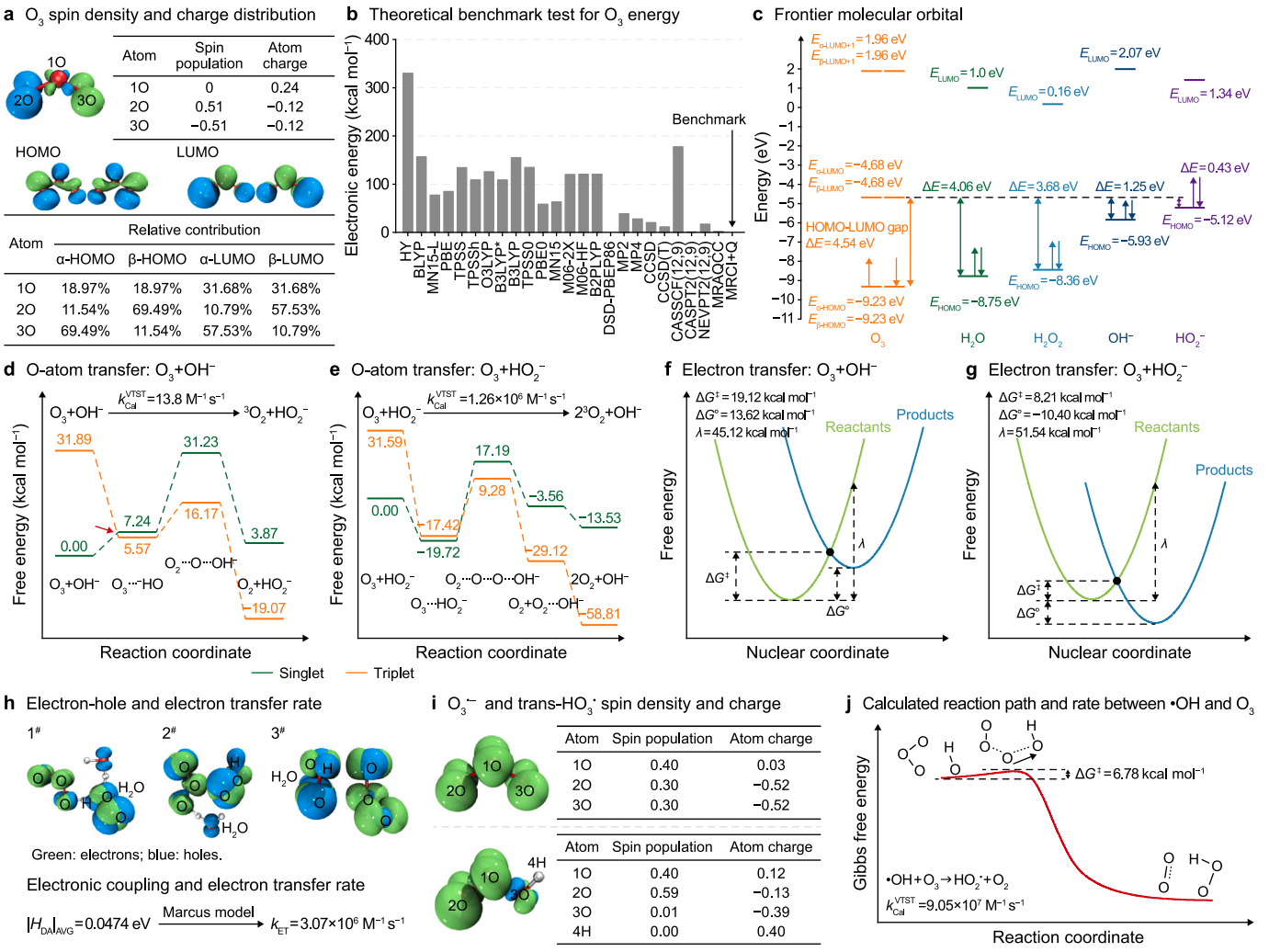

Fig. 5. Thermodynamic and kinetic calculations of the potential mechanism of O_3 with OH^- and HO_2^-. (**a**), Spin density, charge distribution, and frontier-orbital contributions for O_3. **b**, Benchmarking of electronic-structure methods for the calculated energy of O_3. **c**, Frontier molecular orbital energies of O_3, H_2O, H_2O_2, OH^-, and HO_2^-. **d**–**e**, Calculated free-energy profiles for O-atom transfer in the reactions of O_3 with OH^- (**d**) and HO_2^- (**e**). **f**–**g**, Marcus analysis of electron transfer in the reactions of O_3 with OH^- (**f**) and HO_2^- (**g**). In panel **d**, the red arrow points to the singlet-triplet spin crossover. **h**, Electron–hole distribution, electronic coupling, and calculated electron-transfer rate. **i**, Spin density and atomic charge distributions of $O_3^{\bullet-}$ and trans-$HO_3^{\bullet}$. **j**, Calculated reaction pathway and rate constant for the reaction of •OH with O_3.

interaction [62]. Therefore, considering the O_3/OH^- and O_3/HO_2^- processes, the addition reaction as the rate-determining step for is thermodynamically implausible, and it is more likely to be complexes rather than adducts. Complexes (not adducts) likely form initially, and the originally suggested mechanism of O-atom transfer and ET may be feasible but requires further validation or refinement.

3.5.2. *Oxygen-atom transfer mechanism of O_3 with OH^- and HO_2^-*

For the reaction of O_3 with OH^-, O-atom transfer, as the first step, must solve the spin-forbidden transition [16]. Two-state reactivity (TSR) theory was applied to investigate the spin-inversion process during the rate-determining step [63,64]. The singlet-triplet potential energy surfaces intersected, and spin inversion preceded the transition state (Fig. 5d). Breaking the O_3 electronic configuration caused spin inversion, resulting in a triplet state emerging as the ground state. There is no crossing between the triplet and singlet potential energy surfaces during product formation, so this O-atom transfer process is irreversible. Variational transition state theory (VTST) calculation further revealed the rate constant of $k_{OH,\ O_3}^{-} = 13.80\ M^{-1}\ s^{-1}$, compared with the experimental value of 70 $M^{-1}\ s^{-1}$ (Supplementary Text S3) [65]. In addition, electrostatically induced intermolecular hydrogen bonding between O_3 and OH^- (Supplementary Fig. S16) and altered the electronic configuration (Supplementary Fig. S17). The intrinsic reaction coordinate (IRC) recorded two-state reactivity (Fig. 5d and Supplementary Table S8) [66], and triplet $O_3(O(^3P) + O_2(^3\Sigma_g^-))$ transferred the two-electron O-atom to OH^- to produce HO_2^- and released $^3O_2(^3\Sigma_g^-)$) (equation (25)). The essence of spin inversion is the spin-orbit coupling (SOC) caused by the relativistic effect, while the unique properties of O_3 with antiferromagnetic coupling (SOC $\propto Z^4$, Z represents atomic number) and the admixture of a higher spin state in the ground state are both accountable for spin inversion. For the O_3/HO_2^- initial reaction, the O-atom transfer also proceeded (Fig. 5e), in which the calculated O-atom transfer rate was $1.26 \times 10^6\ M^{-1}\ s^{-1}$ at 20 °C (equation (26)). The calculation identified the key structures on the reaction minimum energy path (Supplementary Fig. S18), and

formed an intermolecular H-bond complex between O_3 and HO_2^- (Supplementary Fig. S19).

3.5.3. Electron transfer mechanism insight of O_3 with OH^- and HO_2^-

While O-atom transfer alone does not trigger radical chains, ET is the root that induces free radical generation (equations (27) and (28)). We calculated the ET rate constant using Marcus theory (equations (29) and (30), Supplementary Text S4) [67,68]. First, the calculated Gibbs free energy changes (ΔG°) were −10.40 and + 13.62 kcal mol^{-1} for equations (27) and (28), respectively. Then, solvent reorganization energies were calculated, yielding an ET energy barrier ($\Delta G^\ddagger$) of +19.12 kcal mol^{-1} (Fig. 5f), making direct •OH formation thermodynamically unfavorable via ET. In contrast, the reverse process of O_3/OH^- is thermodynamically and kinetically feasible, as has been experimentally confirmed [69]. The generation of HO_2^- in equation (25) was determined as the sole initial reaction in the O_3/OH^- system. However, for the O_3/HO_2^- reaction, the ET occurred from the electron donor HO_2^- to acceptor O_3, and the total reorganization energy obtained was 51.54 kcal mol^{-1}, resulting in the ET energy barrier reaching ΔG° = 8.21 kcal mol^{-1} (Supplementary Table S9–S10).

We further drew the ET potential energy surface (Fig. 5g). Meanwhile, the three charge transfer states of wavefunction coupling were found (Fig. 5h), their respective Boltzmann distributions were calculated [19], and the ET rate constant was eventually determined (Supplementary Text S4). We calculated the ET rate between O_3 and HO_2^-, k_{ET} = 3.07 × 10^6 M^{-1} s^{-1} at 20 °C, and thus the $(k_{O_3,\ HO_2^-})_{total} = k_{O\text{-transfer}} + k_{ET}$ = 4.33 × 10^6 M^{-1} s^{-1} at 20 °C (experimental value k = (5.5–9.6) × 10^6 M^{-1} s^{-1}). Excluding the $HO_2^\bullet/O_2^{\bullet-}$ by the scavenger, the chain propagation medium $O_2^{\bullet-}$ produced would react with O_3 at a rapid rate via ET to generate $O_3^{\bullet-}$. Specifically, the $O_3^{\bullet-}$ generation is collectively contributed by chain and chain propagation in a chain cycle process, and the measured average •OH yield of the three methods was $\Phi_{Average}(O_3/HO_2^-)$ = 67.4%, from which a value of $k_{ET} \approx k_{O\text{-atom}}$ = 2.75 × 10^6 M^{-1} s^{-1} was derived (substituting Φ = 67.4% gives k_{ET}:$k_{O\text{-atom}}$ = 50.8%:49.2%). The results demonstrated that the rates of these two processes should be nearly identical within the margin of error, confirming the presence of dual initiation routes. The initiation reactions of O_3 decay induced by OH^- and HO_2^- are proposed as equations (25)–(27) and equations (26) and (27), respectively:

$$O_3 + OH^- \rightarrow O_2\left(^3\Sigma_g^-\right) + HO_2^- \quad (25)$$

$$O_3 + HO_2^- \rightarrow 2O_2\left(^3\Sigma_g^-\right) + OH^- \quad (26)$$

$$O_3 + HO_2^- \rightarrow O_3^{\bullet-} + HO_2^\bullet \quad (27)$$

$$O_3 + OH^- \rightarrow O_3^{\bullet-} + HO\cdot \quad (28)$$

$$k = \frac{V^2}{\hbar} \times \sqrt{\frac{\pi}{\lambda k_B T}} \times \exp\left[\frac{-\Delta G^\ddagger}{k_B T}\right] \quad (29)$$

$$\Delta G^\ddagger = \frac{(\Delta G^\circ + \lambda)^2}{4\lambda} \quad (30)$$

3.5.4. $pK_a(HO_3^\bullet/O_3^{\bullet-})$ calculation and O_3 chain decay mechanism

Except for the initiation process, we further calculated the rate of •OH and O_3 in aqueous solution. However, before this, it was crucial to determine the ambiguous pK_a of $HO_3^\bullet$ with a trans structure [70], which was determined to be 6.15 and later modified to −2 [16,37,71]. We found that this value should be close to neutral, and that the original 6.15 was reasonable rather than a "kinetic" pK_a [14]; the charge analysis and thermodynamic cycle calculations provide evidence for this. The intramolecular π bond was observed in the $O_3^{\bullet-}$ and $HO_3^\bullet$ (Supplementary Fig. S20–S21). The atom charges of H_2O_2, $HO_2^\bullet$, and HO_2^- connected to hydroxyl groups are negative, while the central O-atom charges in $O_3^{\bullet-}$ and $HO_3^\bullet$ are positive like O_3 (Fig. 5i), limiting its contribution to solvation free energy (Supplementary Table S11 and Fig. S22). Therefore, $HO_3^\bullet$ does not conform to the linear fitting of the "increasing O-atom numbers and decreasing the pK_a" in H_xO_y, and our fitting value is $pK_a(HO_3^\bullet/O_3^{\bullet-})$ = 6.66. Another rigorous thermodynamic calculation yields $pK_a(HO_3^\bullet/O_3^{\bullet-})$ = 7.56 (equations (31) and (32), Supplementary Fig. S23). As all favorable evidence points to the fact that $pK_a(HO_3^\bullet/O_3^{\bullet-})$ must be around neutral, perhaps we should accept $pK_a(HO_3^\bullet/O_3^{\bullet-})$ = 6.15 again.

$$pK_a = \frac{\Delta G_a^\circ(aq)}{2.3026RT} \quad (31)$$

$$\Delta G_a^\circ(aq) = G^\circ(H^+, aq) + G^\circ(A^-, aq) - G^\circ(HA, aq) \quad (32)$$

where G°(aq) is the standard Gibbs free energy in aqueous solution, R denotes the gas constant (R = 8.314 J mol^{-1} K^{-1}), and T refers to thermodynamic temperature (K). Then, the rate constant between •OH and O_3 mentioned above is more likely to be 1.1 × 10^8 M^{-1} s^{-1} in aqueous solution [72], while the rate is widely accepted as 4.4 × 10^7 M^{-1} s^{-1} in the gas phase [73]. For a non-proton-involved reaction, reaction rates in the gas and liquid phases are generally comparable. Indeed, our result proved the rate reliability through strict VTST calculations (Fig. 5j), yielding $k_{•OH,\ O_3}$ = 9.05 × 10^7 M^{-1} s^{-1} at 20 °C. Furthermore, we speculate that this rate should be relatively slow, and at least far from the diffusion rate, because the reaction is a two-electron O-atom transfer process involving free radicals, and the energy barrier is

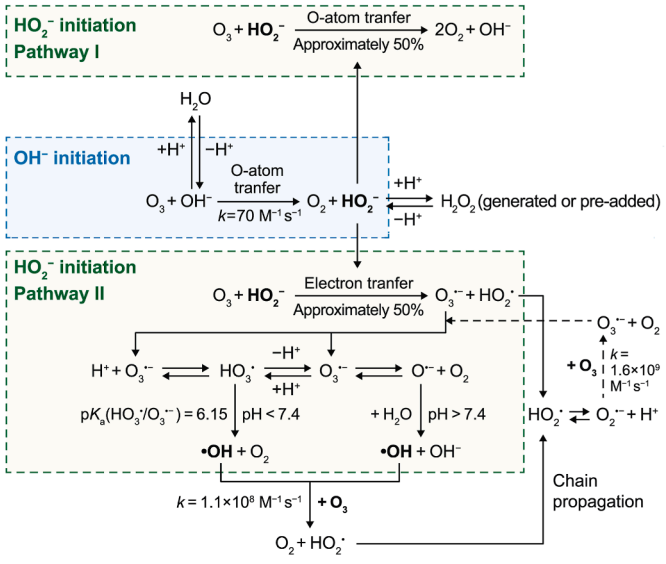

Fig. 6. Proposed mechanism for O_3 attenuation with OH^- and HO_2^-. OH^- initiates O_3 decay through O-atom transfer to generate HO_2^-, which can also be supplied by added or *in situ*-generated H_2O_2. HO_2^- then reacts with O_3 through two competing pathways of comparable contribution: O-atom transfer to form O_2 and OH^-, and electron transfer to form $O_3^{\bullet-}$ and $HO_2^\bullet$, followed by chain propagation and •OH formation. The acid–base equilibria among $HO_3^\bullet$, $O_3^{\bullet-}$, and $HO_2^\bullet/O_2^{\bullet-}$ determine the dominant radical pathway as a function of pH. Selected rate constants and pK_a values are indicated in the scheme.

significantly higher than that for a single ET rate. Therefore, this rate is $k \ll 10^9\ M^{-1}\ s^{-1}$ (Supplementary Fig. S24). We summarized and proposed the revised mechanism of O_3 attenuation induced by the OH^- and HO_2^- based on the established research (Fig. 6).

The O_3 chain decay in H_2O or H_2O_2 reactivity proceeds as follows: O_3 oxidizes OH^- to HO_2^- via O-atom transfer, which constitutes the rate-limiting step of OH^--inducing O_3 decay ($k = 70\ M^{-1}\ s^{-1}$, calculation value $k_{calculation} = 13.8\ M^{-1}\ s^{-1}$). The *in situ* generated or externally added HO_2^- reduces O_3 to O_2 through a non-radical pathway, or to $O_3^{\bullet-}$ through a free radical pathway. These two competing pathways proceeded at comparable rates ($k \approx 2.75 \times 10^6\ M^{-1}\ s^{-1}$); the calculated values are 1.26×10^6 and $3.07 \times 10^6\ M^{-1}\ s^{-1}$, respectively. These correspond to O-atom transfer accompanied by spin flip and ET involving electron transition. Notably, the ET leads to O_3 chain initiation and generates •OH precursor $O_3^{\bullet-}$. The fate of $O_3^{\bullet-}$ is to establish two equilibria, one path is the equilibrium between $O_3^{\bullet-}$ with $O^{\bullet-}$ and O_2 ($k = 1.94 \times 10^3\ s^{-1}$), and another is the protonation equilibrium process ($pK_a(HO_3^{\bullet}/O_3^{\bullet-}) = 6.15$, calculated value $pK_a(HO_3^{\bullet}/O_3^{\bullet-}) = 6.66$ and 7.56). Moreover, the chain promoter $O_2^{\bullet-}$ is simultaneously formed in the initiation reaction, which reduces O_3 and further generates $O_3^{\bullet-}$, resulting in an approximately 67 % •OH yield in a complete chain process.

4. Conclusions

This study systematically investigates the kinetics and mechanism of •OH formation in aqueous solution, where OH^- and HO_2^- initiated O_3. Adding H_2O_2 to the O_3 aqueous solution is recognized as one of the most economical and effective methods for enhancing treatment efficiency. Although an increased pH is a theoretically feasible approach for promoting •OH generation, it is impractical in applications, as evidenced by the observed acceleration of pollutant degradation rates and the significant enhancement of •OH production under such conditions. The •OH yield in the peroxone reaction was approximately 67%, surpassing the previously reported 50%. By integrating Marcus ET theory and transition-state theories, we proposed a revised mechanistic framework: O_3 with biradical property facilitates singlet-triplet state crossover, and imposed spin-orbit coupling induces spin inversion from the singlet to the triplet state. Spin-flipped triplet $O_3(O(^3P) + O_2(^3\Sigma_g^-))$ underwent O-atom transfer to OH^-, formed HO_2^- and released $O_2(^3\Sigma_g^-)$; Subsequently, either generated or pre-added, HO_2^- initiated O_3 radical chain reaction via an ET pathway (approximately 50% of the total rate in peroxone reaction) and O-atom transfer process accompanied by the release of $O_2(^3\Sigma_g^-)$ (approximately 50% of peroxone reaction). Furthermore, the p*K*a of $HO_3^{\bullet}/O_3^{\bullet-}$ must be near neutral because of the limited contribution of the central positively charged O-atom to the free energy of the solvent. The rate constant for the O-atom transfer reaction between •OH and O_3 was quantified as $1.1 \times 10^8\ M^{-1}\ s^{-1}$, resolving previous uncertainties. Collectively, these findings clarified and revised the mechanism by which the OH^- and HO_2^--triggered O_3 chain decay and •OH-mediated oxidation, providing a robust theoretical insight for optimizing O_3-based advanced oxidation processes in water treatment applications.

CRediT authorship contribution statement

Yishi Wang: Writing – review & editing, Writing – original draft, Visualization, Methodology, Investigation. **Wei Qiu:** Writing – review & editing, Supervision, Project administration, Conceptualization. **Yongbo Yu:** Writing – review & editing, Formal analysis. **Jun Ma:** Writing – review & editing, Project administration, Funding acquisition.

Declaration of competing interest

Dr. Jun Ma, an Advisory Board Member of Environmental Science and Ecotechnology, was not involved in the editorial review or the decision to publish this article. The other authors declare that they have no known competing financial interests or personal relationships that could have appeared to influence the work reported in this paper.

Acknowledgments

We thank the financial support by the National Natural Science Foundation of China (NFSC20240010) and State Key Laboratory of Urban-rural Water Resources and Environment, Harbin Institute of Technology (No. 2025DX23).

Appendix A. Supplementary data

Supplementary data to this article can be found online at https://doi.org/10.1016/j.ese.2026.100704.

References

[1] E. Miliordos, S.S. Xantheas, On the bonding nature of ozone (O_3) and its sulfur-substituted analogues SO_2, OS_2, and S_3: correlation between their biradical character and molecular properties, J. Am. Chem. Soc. 136 (7) (2014) 2808–2817.
[2] A. Kalemos, A. Mavridis, Electronic structure and bonding of ozone, J. Chem. Phys. 129 (5) (2008) 054312.
[3] S.E. Wheeler, D.H. Ess, K.N. Houk, Thinking out of the black box: accurate barrier heights of 1,3-dipolar cycloadditions of ozone with acetylene and ethylene, J. Phys. Chem. A 112 (8) (2008) 1798–1807.
[4] I.B. Bersuker, Jahn–Teller and Pseudo-Jahn–Teller effects: from particular features to general tools in exploring molecular and solid state properties, Chem. Rev. 121 (3) (2021) 1463–1512.
[5] A.J. Cohen, M. Brauer, R. Burnett, H.R. Anderson, J. Frostad, K. Estep, K. Balakrishnan, B. Brunekreef, L. Dandona, R. Dandona, V. Feigin, G. Freedman, B. Hubbell, A. Jobling, H. Kan, L. Knibbs, Y. Liu, R. Martin, L. Morawska, C.A. Pope, H. Shin, K. Straif, G. Shaddick, M. Thomas, R. van Dingenen, A. van Donkelaar, T. Vos, C.J.L. Murray, M.H. Forouzanfar, Estimates and 25-year trends of the global burden of disease attributable to ambient air pollution: an analysis of data from the Global Burden of Diseases Study 2015, Lancet 389 (10082) (2017) 1907–1918.
[6] S. Lim, J.L. Shi, U. von Gunten, D.L. McCurry, Ozonation of organic compounds in water and wastewater: a critical review, Water Res. 213 (2022) 118053.
[7] D. Wang, Y. Xing, J. Li, F. Dong, H. Cheng, Z. He, L. Wang, S. Giannakis, S. Song, J. Ma, Degradation of odor compounds in drinking water by ozone and ozone-based advanced oxidation processes: a review, ACS ES&T Wat 3 (11) (2023) 3452–3473.
[8] W. Ding, W. Jin, S. Cao, X. Zhou, C. Wang, Q. Jiang, H. Huang, R. Tu, S.-F. Han, Q. Wang, Ozone disinfection of chlorine-resistant bacteria in drinking water, Water Res. 160 (2019) 339–349.
[9] Y. Yang, J. Jiang, X. Lu, J. Ma, Y. Liu, Production of sulfate radical and hydroxyl radical by reaction of ozone with peroxymonosulfate: a novel sdvanced oxidation process, Environ. Sci. Technol. 49 (12) (2015) 7330–7339.
[10] J. Staehelin, J. Hoigne, Decomposition of ozone in water: rate of initiation by hydroxide ions and hydrogen peroxide, Environ. Sci. Technol. 16 (10) (1982) 676–681.
[11] J. Hoigné, H. Bader, W.R. Haag, J. Staehelin, Rate constants of reactions of ozone with organic and inorganic compounds in water—III. Inorganic compounds and radicals, Water Res. 19 (8) (1985) 993–1004.
[12] U. von Gunten, Oxidation processes in water treatment: are we on track? Environ. Sci. Technol. 52 (9) (2018) 5062–5075.
[13] D.B. Miklos, C. Remy, M. Jekel, K.G. Linden, J.E. Drewes, U. Hübner, Evaluation of advanced oxidation processes for water and wastewater treatment – a critical review, Water Res. 139 (2018) 118–131.
[14] G. Merényi, J. Lind, S. Naumov, C.v. Sonntag, Reaction of ozone with hydrogen peroxide (peroxone process): a revision of current mechanistic concepts based on thermokinetic and quantum-chemical considerations, Environ. Sci. Technol. 44 (9) (2010) 3505–3507.
[15] A. Fischbacher, J. von Sonntag, C. von Sonntag, T.C. Schmidt, The •OH radical yield in the $H_2O_2 + O_3$ (Peroxone) reaction, Environ. Sci. Technol. 47 (17) (2013) 9959–9964.
[16] G. Merényi, J. Lind, S. Naumov, C. von Sonntag, The reaction of ozone with the hydroxide ion: mechanistic considerations based on thermokinetic and quantum chemical calculations and the role of HO_4^- in superoxide dismutation, Chem. Eur J. 16 (4) (2010) 1372–1377.
[17] J.M. Anglada, M. Torrent-Sucarrat, M.F. Ruiz-Lopez, M. Martins-Costa, Is the

HO_4^- anion a key species in the aqueous-phase decomposition of ozone? Chem. Eur J. 18 (42) (2012) 13435–13445.
[18] P. Zhang, Y. Yang, X. Duan, Y. Liu, S. Wang, Density functional theory calculations for Insight into the heterocatalyst reactivity and mechanism in persulfate-based advanced oxidation reactions, ACS Catal. 11 (17) (2021) 11129–11159.
[19] S. Tan, R. Wang, K. Wang, Z. Yang, Y. Chen, Y. Zhang, Unravelling the structure-dependent defluorination mechanisms of per- and polyfluoroalkyl substances by hydrated electrons in UV/sulfite, Nat. Water 3 (6) (2025) 734–745.
[20] H. Bader, J. Hoigné, Determination of ozone in water by the indigo method, Water Res. 15 (4) (1981) 449–456.
[21] H. Bader, V. Sturzenegger, J. Hoigné, Photometric method for the determination of low concentrations of hydrogen peroxide by the peroxidase catalyzed oxidation of N,N-diethyl-p-phenylenediamine (DPD), Water Res. 22 (9) (1988) 1109–1115.
[22] F. Neese, Software update: the ORCA program system—Version 5.0 12 (5) (2022) e1606.
[23] T. Lu, A comprehensive electron wavefunction analysis toolbox for chemists, Multiwfn, J. Chem. Phys. 161 (8) (2024) 082503.
[24] T. Lu, F. Chen Multiwfn, A multifunctional wavefunction analyzer, J. Comput. Chem. 33 (5) (2012) 580–592.
[25] T. Lu, Q. Chen, A simple method of identifying π orbitals for non-planar systems and a protocol of studying π electronic structure, Theor. Chem. Acc. 139 (2) (2020) 25.
[26] T. Lu. Molclus Program. Version 1.12. http://www.keinsci.com/research/molclus.html. (Accessed on March 4, 2025).).
[27] W. Humphrey, A. Dalke, K. Schulten, VMD: visual molecular dynamics, J. Mol. Graphics Modell. 14 (1) (1996) 33–38.
[28] L. Linxiang, Y. Abe, Y. Nagasawa, R. Kudo, N. Usui, K. Imai, T. Mashino, M. Mochizuki, N. Miyata, An HPLC assay of hydroxyl radicals by the hydroxylation reaction of terephthalic acid, Biomed. Chromatogr. 18 (7) (2004) 470–474.
[29] J. Staehelin, R.E. Buehler, J. Hoigne, Ozone decomposition in water studied by pulse radiolysis. 2. Hydroxyl and hydrogen tetroxide (HO_4) as chain intermediates, J. Phys. Chem. 88 (24) (1984) 5999–6004.
[30] L. Forni, D. Bahnemann, E.J. Hart, Mechanism of the hydroxide ion-initiated decomposition of ozone in aqueous solution, J. Phys. Chem. 86 (2) (1982) 255–259.
[31] J. Staehelin, J. Hoigne, Decomposition of ozone in water in the presence of organic solutes acting as promoters and inhibitors of radical chain reactions, Environ. Sci. Technol. 19 (12) (1985) 1206–1213.
[32] Y. Guo, G. Yu, U. von Gunten, Y. Wang, Evaluation of the role of superoxide radical as chain carrier for the formation of hydroxyl radical during ozonation, Water Res. 242 (2023) 120158.
[33] J.L. Acero, K. Stemmler, U. von Gunten, Degradation kinetics of atrazine and its degradation products with ozone and OH radicals: a predictive tool for drinking water treatment, Environ. Sci. Technol. 34 (4) (2000) 591–597.
[34] G.V. Buxton, C.L. Greenstock, W.P. Helman, A.B. Ross, Critical Review of rate constants for reactions of hydrated electrons, hydrogen atoms and hydroxyl radicals (·OH/·O−) in aqueous solution, J. Phys. Chem. Ref. Data 17 (2) (1988) 513–886.
[35] D. Bahnemann, E.J. Hart, Rate constants of the reaction of the hydrated electron and hydroxyl radical with ozone in aqueous solution, J. Phys. Chem. 86 (2) (1982) 252–255.
[36] K. Sehested, J. Holcman, E. Bjergbakke, E.J. Hart, A pulse radiolytic study of the reaction hydroxyl + ozone in aqueous medium, J. Phys. Chem. 88 (18) (1984) 4144–4147.
[37] R.E. Buehler, J. Staehelin, J. Hoigne, Ozone decomposition in water studied by pulse radiolysis. 1. $HO_2^•/O_2^{•-}$ and $HO_3^•/O_3^{•-}$ as intermediates, J. Phys. Chem. 88 (12) (1984) 2560–2564.
[38] M.M. Sein, A. Golloch, T.C. Schmidt, C. von Sonntag, No marked kinetic isotope effect in the peroxone ($H_2O_2/D_2O_2+O_3$) reaction: mechanistic consequences, ChemPhysChem 8 (14) (2007) 2065–2067.
[39] T.M. Lesko, A.J. Colussi, M.R. Hoffmann, Hydrogen isotope effects and mechanism of aqueous ozone and peroxone decompositions, J. Am. Chem. Soc. 126 (13) (2004) 4432–4436.
[40] M.S. Elovitz, U. von Gunten, Hydroxyl radical/ozone ratios during ozonation processes. I. The Rct concept, Ozone Sci. Eng. 21 (3) (1999) 239–260.
[41] Y. Lei, Y. Yu, X. Lei, X. Liang, S. Cheng, G. Ouyang, X. Yang, Assessing the use of probes and quenchers for understanding the reactive species in advanced oxidation processes, Environ. Sci. Technol. 57 (13) (2023) 5433–5444.
[42] S. Goldstein, D. Aschengrau, Y. Diamant, J. Rabani, Photolysis of aqueous H_2O_2: Quantum yield and applications for polychromatic UV actinometry in photoreactors, Environ. Sci. Technol. 41 (21) (2007) 7486–7490.
[43] J. Hoigné, H. Bader, Rate constants of reactions of ozone with organic and inorganic compounds in water—I: Non-dissociating organic compounds, Water Res. 17 (2) (1983) 173–183.
[44] P. Ulanski, C. von Sonntag, The OH radical-induced chain reactions of methanol with hydrogen peroxide and with peroxodisulfate, Journal of the Chemical Society-Perkin Transactions 2 (2) (1999) 165–168.
[45] Y. Liu, J. Jiang, J. Ma, Y. Yang, C. Luo, X. Huangfu, Z. Guo, Role of the propagation reactions on the hydroxyl radical formation in ozonation and peroxone (ozone/hydrogen peroxide) processes, Water Res. 68 (2015) 750–758.
[46] M.N. Schuchmann, C. Von Sonntag, Hydroxyl radical-induced oxidation of 2-methyl-2-propanol in oxygenated aqueous solution. A product and pulse radiolysis study, J. Phys. Chem. 83 (7) (1979) 780–784.
[47] R. Flyunt, A. Leitzke, G. Mark, E. Mvula, E. Reisz, R. Schick, C. von Sonntag, Determination of •OH, $O_2^{•-}$, and hydroperoxide yields in ozone reactions in aqueous solution, J. Phys. Chem. B 107 (30) (2003) 7242–7253.
[48] J. Hoigné, H. Bader, The role of hydroxyl radical reactions in ozonation processes in aqueous solutions, Water Res. 10 (5) (1976) 377–386.
[49] K. Sehested, H. Corfitzen, J. Holcman, E.J. Hart, On the mechanism of the decomposition of acidic O_3 solutions, thermally or H_2O_2-initiated, J. Phys. Chem. A 102 (16) (1998) 2667–2672.
[50] M.G. Steiner, C.F. Babbs, Quantitation of the hydroxyl radical by reaction with dimethyl sulfoxide, Arch. Biochem. Biophys. 278 (2) (1990) 478–481.
[51] D. Veltwisch, E. Janata, K.-D. Asmus, Primary processes in the reaction of OH··-radicals with sulphoxides, Journal of the Chemical Society-Perkin Transactions 2 (1) (1980) 146–153.
[52] W.A. Pryor, D.H. Giamalva, D.F. Church, Kinetics of ozonation. 2. Amino acids and model compounds in water and comparisons to rates in nonpolar solvents, J. Am. Chem. Soc. 106 (23) (1984) 7094–7100.
[53] T.J. Lee, P.R. Taylor, A diagnostic for determining the quality of single-reference electron correlation methods, Int. J. Quantum Chem 36 (S23) (1989) 199–207.
[54] Y. Zhao, O. Tishchenko, J.R. Gour, W. Li, J.J. Lutz, P. Piecuch, D.G. Truhlar, Thermochemical kinetics for multireference systems: addition reactions of ozone, J. Phys. Chem. A 113 (19) (2009) 5786–5799.
[55] H. Lischka, D. Nachtigallová, A.J.A. Aquino, P.G. Szalay, F. Plasser, F.B.C. Machado, M. Barbatti, Multireference approaches for excited states of molecules, Chem. Rev. 118 (15) (2018) 7293–7361.
[56] S. Naumov, C. von Sonntag, Quantum chemical studies on the formation of ozone adducts to aromatic compounds in aqueous solution, Ozone Sci. Eng. 32 (1) (2010) 61–65.
[57] M.C. Garner, K.A. Hanold, M.S. Resat, R.E. Continetti, Stability and dissociation dynamics of the low-lying excited states of ozone, J. Phys. Chem. A 101 (36) (1997) 6577–6582.
[58] S.M. Anderson, K. Mauersberger, Ozone absorption spectroscopy in search of low-lying electronic states, J. Geophys. Res.-Atmos. 100 (D2) (1995) 3033–3048.
[59] T.Y. Takeshita, B.A. Lindquist, T.H. Dunning Jr., Insights into the electronic structure of ozone and sulfur dioxide from generalized valence bond theory: bonding in O_3 and SO_2, J. Phys. Chem. A 119 (28) (2015) 7683–7694.
[60] J.R. Kanofsky, P. Sima, Singlet oxygen production from the reactions of ozone with biological molecules, J. Biol. Chem. 266 (14) (1991) 9039–9042.
[61] J. Gu, Y. Yang, Y. Song, J. Jiang, Theoretical insight into the initial reaction of ozone with peroxide: single electron transfer or adduct formation, Chem. Eng. J. 429 (2022) 132308.
[62] D. Trogolo, J.S. Arey, P.R. Tentscher, Gas-Phase ozone reactions with a structurally diverse set of molecules: barrier heights and reaction energies evaluated by coupled cluster and density functional theory calculations, J. Phys. Chem. A 123 (2) (2019) 517–536.
[63] A.R. Reddy, M. Bendikov, Diels–Alder reaction of acenes with singlet and triplet oxygen – theoretical study of two-state reactivity, Chem. Commun. (11) (2006) 1179–1181.
[64] D. Schröder, S. Shaik, H. Schwarz, Two-state reactivity as a new concept in organometallic chemistry, Acc. Chem. Res. 33 (3) (2000) 139–145.
[65] A. Fernández-Ramos, J.A. Miller, S.J. Klippenstein, D.G. Truhlar, Modeling the kinetics of bimolecular reactions, Chem. Rev. 106 (11) (2006) 4518–4584.
[66] B. Yang, L. Gagliardi, D.G. Truhlar, Transition states of spin-forbidden reactions, Phys. Chem. Chem. Phys. 20 (6) (2018) 4129–4136.
[67] E.J. Piechota, G.J. Meyer, Introduction to electron transfer: theoretical foundations and pedagogical examples, J. Chem. Educ. 96 (11) (2019) 2450–2466.
[68] R.A. Marcus, Electron transfer reactions in chemistry: theory and experiment (Nobel Lecture), Angew. Chem. Int. Ed. 32 (8) (1993) 1111–1121.
[69] K. Sehested, J. Holcman, E. Bjergbakke, E.J. Hart, Formation of ozone in the reaction of hydroxyl with O_3^- and the decay of the ozonide ion radical at pH 10-13, J. Phys. Chem. 88 (2) (1984) 269–273.
[70] K. Suma, Y. Sumiyoshi, Y. Endo, The rotational spectrum and structure of the HOOO radical, Science 308 (5730) (2005) 1885–1886.
[71] S. Naumov, C. von Sonntag, The reaction of •OH with O_2, the decay of $O_3^{•-}$ and the pKa of $HO_3^•$–interrelated questions in aqueous free-radical chemistry, J. Phys. Org. Chem. 24 (7) (2011) 600–602.
[72] K. Sehested, J. Holcman, E. Bjergbakke, E.J. Hart, Use of pulse-radiolysis for the study of the chemistry of aqueous ozone and ozonide solutions, J. Radioanal. Nucl. Chem. 101 (2) (1986) 239–250.
[73] R. Atkinson, D.L. Baulch, R.A. Cox, J.N. Crowley, R.F. Hampson, R.G. Hynes, M.E. Jenkin, M.J. Rossi, J. Troe, Evaluated kinetic and photochemical data for atmospheric chemistry: volume I - gas phase reactions of O_x, HO_x, NO_x and SO_x species, Atmos. Chem. Phys. 4 (2004) 1461–1738.